Synergistic Optimization of Electronic Structure and Defects via Light Zn-Doping for High Performance n-Type $Bi_2(Te, Se)_3$ Thermoelectrics in Cooling and Power Generation

Jiayi Peng(彭佳怡)[1†], Shulin Bai(白树林)[1,2,3†], Dongrui Liu(刘东锐)[1], Yi Wen(文熠)[1], Yixuan Hu(胡艺轩)[1], Pengpeng Chen(陈鹏鹏)[1], Dezheng Gao(高德政)[1], Lei Wang(王磊)[1], Suyao Liu(刘苏瑶)[1], Huiqiang Liang(梁会强)[4], Xu Liu(刘旭)[1], Yanling Pei(裴延玲)[1], Qing Tan(谭晴)[1*], Bingchao Qin(秦炳超)[1,2,3*], and Li-Dong Zhao(赵立东)[1,2,3*]

[1]*State Key Laboratory of Special Materials Surface Engineering, School of Materials Science and Engineering, Beihang University, Beijing 100191, China*
[2]*Center for Bioinspired Science and Technology, Hangzhou International Innovation Institute, Beihang University, Hangzhou 311115, China*
[3]*Tianmushan Laboratory, Beihang University, Hangzhou 311115, China*
[4]*Hebei Key Laboratory of Optic-Electronic Information and Materials, College of Physics Science and Technology, Hebei University, Baoding 071002, China*

(Received 22 January 2026; accepted manuscript online 5 February 2026)

The interdependence of electrical parameters has long inhibited the progress of bismuth telluride (Bi_2Te_3), limiting its widespread application in thermoelectric cooling and power generation. This work investigates the n-type $Bi_2Te_{2.79}Se_{0.21}I_{0.004}$ ($Bi_2(Te, Se)_3$, BTS) system with light Zn doping, revealing that Zn addition simultaneously enhances the Seebeck coefficient (S) and electrical conductivity (σ) through the modulation of defect composition and multi-level band regulation. The substitution of Zn atoms at Bi sites enhances S via bandgap (E_g) widening, band flattening, and band splitting effects, contributing to a competitive power factor (PF) of $\sim$60 $\mu W \cdot cm^{-1} \cdot K^{-2}$. Additionally, thermal conductivity is maintained at a low level, leading to an extraordinary figure-of-merit (ZT) value of $\sim$1.3 at room temperature. Furthermore, the $Bi_2Zn_{0.01}Te_{2.79}Se_{0.21}I_{0.004}$ system demonstrates impressive thermoelectric device performance, with a maximum cooling temperature difference (ΔT_{max}) of $\sim$70.0 K at 300 K, rising to $\sim$78.0 K at 323 K and $\sim$85.7 K at 343 K, as well as a maximum conversion efficiency (η_{max}) of $\sim$6.2% under a ΔT of 200 K. This study clarifies the mechanism of Zn doping and presents a cost-effective strategy for enhancing the performance of n-type BTS thermoelectrics and their devices.

DOI: 10.1088/0256-307X/43/3/030803 CSTR: 32039.14.0256-307X.43.3.030803

1. Introduction. The accelerating global transition to the 6G era has intensified pressures from energy scarcity and environmental pollution, driving an urgent demand for sustainable energy solutions.[1] Thermoelectric materials, capable of directly converting heat into electricity without pollution, have garnered extensive attention for their potential in the field of renewable energy, with their performance assessed by a dimensionless figure-of-merit $ZT = S^2\sigma T/\kappa$, where S (Seebeck coefficient), σ (electrical conductivity), T (absolute temperature), and κ (thermal conductivity) denote the respective physical quantities.[2,3] However, the strong interdependence of thermal and electrical parameters remains a key bottleneck to widespread thermoelectrics deployment. To address these issues, strategies including lattice plainification,[4–6] crystal symmetry modification,[7] band structure engineering,[8–15] and all-scale hierarchical defects[16–20] have been proposed. The past decades have witnessed a large volume of work on thermoelectric materials such as SnSe,[21–27] PbQ (Q = S, Se, Te),[6,28–31] SnS,[32,33] and GeTe.[14,34–37] Despite this broad exploration, Bi_2Te_3 systems still dominate the commercial thermoelectric market, owing to their superior room-temperature thermoelectric performance and exceptional stability, and thus hold tremendous potential for applications in both solid-state cooling and power generation.

Nevertheless, compared to the p-type $(Bi, Sb)_2Te_3$ (BST) systems, the further advancement of n-type $Bi_2(Te, Se)_3$ (BTS) counterparts has been severely restricted because detrimental bipolar diffusion[8] not only degrades the Seebeck coefficient but also maintains a relatively higher thermal conductivity. Therefore, developing effective strategies to upgrade n-type BTS systems is of great significance. Most previous works focused on improving solely thermal or electrical properties by introducing organic or inorganic second phases.[4,9,38–43] Although these

†These authors contributed equally to this work.
*Corresponding authors. Email: tanqing@buaa.edu.cn; qinbingchao@buaa.edu.cn; zhaolidong@buaa.edu.cn
© 2026 Chinese Physical Society and IOP Publishing Ltd. All rights, including for text and data mining, AI training, and similar technologies, are reserved.

second phases optimize thermal conductivity via carrier scattering, they may severely degrade electrical performance and increase the power consumption of cooling devices. Dopants like copper (Cu)[9] and silver (Ag)[4] can strongly enhance electrical properties; yet, a slight change in the dosage of highly active Cu and Ag dopants can cause significant fluctuations in thermoelectric performance, especially in the Seebeck coefficient, making them unsuitable for large-scale commercial production.

Thus, synergistic enhancement in thermoelectric performance turns out to be highly challenging. Moreover, the n-type BTS demonstrates a higher degree of anisotropy than the p-type BST systems, a phenomenon associated with the quasi-layered crystal structure of Bi_2Te_3. As illustrated in Fig. 1(a), BTS is built from hexagonal $Te^{(1)}$–Bi–$Te^{(2)}$–Bi–$Te^{(1)}$ quintuple layers, connected by weak van der Waals interactions between adjacent $Te^{(1)}$ atomic layers. Exploiting this anisotropy demands strongly textured grains, which can be manufactured by novel techniques like liquid-phase hot deformation,[44] layered directional sintering,[8] and layered crystal stacking hot deformation.[45] However, current texturing methods confront critical challenges such as non-uniform grain sizes and complex processing, which increase both cost and labor consumption, thus limiting their scalability. Given these constraints, a more efficient and cost-effective strategy is needed to optimize n-type Bi_2Te_3-based materials for practical applications. The rational optimization of commercially available zone-melted n-type BTS materials emerges as the most feasible near-term solution.

Motivated by the idea that band engineering could serve as a plausible approach for decoupling the electrical parameters (σ and S),[46] and building on the success of Zn doping[47] in p-type BST systems, we investigated the effects of trace Zn incorporation in n-type BTS in this work. Different from prior reports[13,48] that only correlate Zn doping optimization in the n-type BTS system with variations in performance parameters, this study systematically clarifies the optimization mechanism by combining defect evolution and electronic band structure analyses. It further validates the practical applicability of the Zn-doped BTS system via device-level tests, establishing a seamless logical closed loop from performance optimization and microstructural regulation to device applications. More specifically, the results show that Zn doping simultaneously enhances both S and σ values through coordinated modulation of crystal defects and band structure. As Fig. 1(a) illustrates, Zn atoms preferentially occupy Bi sites to form Zn_{Bi} defects, which simultaneously hinder the formation of Bi_{Te} anti-site defects and increase the relative proportion of V_{Te} vacancies, leading to a substantial enhancement in carrier concentration n. Meanwhile, Zn can enhance S due to the widened bandgap E_g, enlarged single-band effective mass m_b^*, and increased band degeneracy N_v resulting from multi-level band regulation (band flattening and splitting effects), as illustrated in Fig. 1(b).

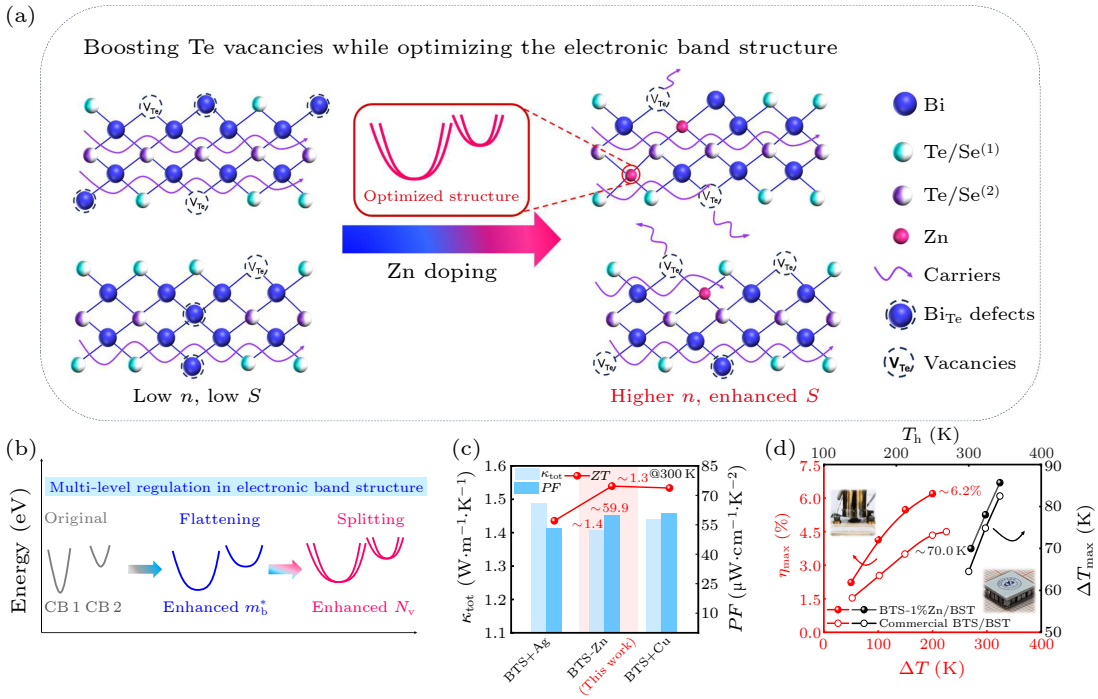

Fig. 1. Internal defect modulation and multi-level band regulation boost thermoelectric performance in commercial n-type BTS. (a) Schematic diagram of the optimization mechanism of n-type Zn-doped BTS. The addition of Zn mainly serves as a substitutional dopant, giving rise to Te vacancies and inhibiting the formation of anti-site defects. The fine-tuned defect combination subtly adjusts carrier concentration while enhancing Seebeck coefficients. (b) The evolution of band structure after Zn doping. (c) Comparison of κ_{tot} values and PF values at 300 K in this work with those of BTS+Ag and BTS+Cu in previous works.[4,9] (d) Maximum cooling temperature difference ΔT_{max} of the full-scale BTS-1.0%Zn/BST-based cooler and maximum conversion efficiency η_{max} of the full-scale BTS-1.0%Zn/BST-based device, alongside corresponding experimental data for commercial BTS-based devices for comparison.

On the other hand, certain dopants like copper (Cu) and silver (Ag) are widely recognized for their capability to notably boost the electrical parameters in Bi_2Te_3 systems. But these enhancements come with a major drawback: the prominently enhanced electron transport also triggers a significant boost in thermal conductivity [Fig. 1(c)]. However, the total thermal conductivity κ_{tot} of BTS-1%Zn is maintained at a low level owing to the intricate adjustments in both defect composition and bandgap. As a consequence, BTS-Zn exhibits a more advantageous thermal contribution from electronic and bipolar parts, holding a lower κ_{tot} of $\sim$1.4 $W{\cdot}m^{-1}{\cdot}K^{-1}$ [Fig. 1(c)]. Along with a compelling increase in the PF value to $\sim$60 $\mu W{\cdot}cm^{-1}{\cdot}K^{-2}$ at 300 K, a peak ZT value of $\sim$1.3 was obtained. Notably, this room-temperature thermoelectric performance surpasses that of the previously reported Cu/Ag-doped BTS system.[4,9]

Moreover, full-scale thermoelectric cooling and power generation devices were assembled by integrating the optimized BTS-1.0%Zn with commercial BST thermoelectrics, as shown in Fig. 1(d). In terms of cooling, the BTS-1.0%Zn/BST-based cooler displays an outstanding maximum cooling temperature difference (ΔT_{max}) of $\sim$70.0 K when the hot-side temperature (T_h) is 303 K, which further rises to $\sim$78.0 K at 323 K and $\sim$85.7 K at 343 K, respectively. Regarding power generation, the measured maximum conversion efficiency (η_{max}) reaches $\sim$6.2% (ΔT = 200 K), exceeding that of commercial devices in both cooling and power generation applications. This work presents a straightforward and effective approach to upgrading the thermoelectric performance of commercial BTS ingots without raising production costs, providing a crucial advancement for n-type BTS thermoelectrics.

2. Results and Discussion.

2.1. Enhancement of Electrical Properties. BTS-x%Zn samples were synthesized (x = 0, 0.2, 0.4, 0.6, 0.8, 1.0, and 1.2) via an improved Bridgman method. The X-ray diffraction (XRD) patterns of the as-prepared samples are presented in Fig. S1 of the Supplementary Materials (SM). All the characteristic peaks match the standard pattern of Bi_2Te_3 (PDF#15-0863), indicating that no other impurities were detected in the BTS-x%Zn samples. Figure 2(a) depicts the lattice parameters obtained from XRD results with different Zn contents. The lattice parameters along the c-axis exhibit a decreasing tendency with increasing Zn content, whereas those along the a-axis remain nearly unchanged, suggesting successful incorporation of Zn into the BTS matrix. With more Zn atoms substituting Bi sites, the lattice parameters along the c-axis decrease progressively from $\sim$30.46 Å (BTS) to $\sim$30.37 Å (BTS-1.2%Zn). This observation can be ascribed to the smaller atomic radius of Zn ($\sim$1.25 Å) in comparison with that of Bi ($\sim$1.46 Å).[13] To verify successful incorporation of Zn into the BTS matrix, X-ray photoelectron spectroscopy (XPS) analysis was performed on the BTS-1.0%Zn sample. Through calibration of the C 1s peak at 284.8 eV in Fig. S2 of the SM, the XPS result in Fig. 2(b) reveals Zn^{2+} peaks at 1022.7 eV (Zn^{2+} $2p_{3/2}$) and 1045.8 eV (Zn^{2+} $2p_{1/2}$),[13] respectively. Zn atoms preferentially occupy Bi sites, forming Zn_{Bi} defects.

Furthermore, the homogeneous distribution of constituent elements in BTS-1%Zn was verified by energy dispersive X-ray spectroscopy (EDS) mapping (Fig. S3 of the SM). Hall measurements were employed to determine the room-temperature carrier concentration n and carrier mobility μ, as shown in Fig. 2(c). The n value increases monotonically as the Zn doping content increases, rising from $\sim 2.84 \times 10^{19}$ cm^{-3} (BTS) to $\sim 4.74 \times 10^{19}$ cm^{-3} (BTS-1.2%Zn). In contrast, the mobility does not follow a monotonic trend: it first increases to $\sim$280.5 $cm^2{\cdot}V^{-1}{\cdot}s^{-1}$ in BTS-0.4%Zn and then gradually decreases to $\sim$106.1 $cm^2{\cdot}V^{-1}{\cdot}s^{-1}$ in BTS-1.2%Zn. To clarify the underlying causes of variations in n and μ, the defect composition before and after Zn doping was analyzed. Zn atoms preferentially substitute Bi sites to form negatively charged substitutional defects (Zn_{Bi}) and bond with Te atoms to form Zn-Te bonds. Given that Zn-Te exhibits a comparatively higher electronegativity difference $\Delta\chi$ than Bi-Te,[13] Zn substitution strengthens the Te bonding interaction, thereby reducing the number of anti-site defects Bi_{Te}. Due to the competitive relationship between Bi_{Te} and Te vacancies (V_{Te}) in BTS systems, the proportion of V_{Te} increases, explaining the rise in n. Consequently, the actual Zn doping concentration can be estimated via the n variation of the BTS-x%Zn samples [Fig. 2(c)]. Higher Zn addition facilitates a more favorable V_{Te} ratio, generating additional free electrons and thereby increasing n. On this basis, the steady rise in n with increasing nominal Zn doping provides compelling verification of the graded increase in the actual Zn doping concentration within the samples. The anomalous μ enhancement in the low Zn doping range (0–0.4%) is ascribed to intricate defect interplay in the n-type BTS system. Since the formation of Zn_{Bi} reduces the density of Bi_{Te}, even though the V_{Te} ratio increases, the beneficial effect of reduced Bi_{Te} on carrier transport outweighs the scattering effect of V_{Te}, thereby boosting μ. With further increases in Zn doping content, the cumulative Zn_{Bi} and V_{Te} defects act as dominant carrier scattering centers and induce intensified lattice distortion, which together result in a gradual decrease in μ [Fig. 2(c)]. Additionally, the elevated carrier concentration exacerbates ionized impurity scattering, further explaining the mobility reduction at high Zn doping levels.

The room-temperature bandgap E_g measurements, as shown in Fig. 2(d), were carried out by infrared spectra. The bandgap increases with increasing Zn content, rising from $\sim$0.16 eV in the BTS matrix to $\sim$0.19 eV in the BTS-1.0%Zn samples. The electronic band structures of Zn-doped Bi_2Te_3 [Fig. 2(e)] and the Bi_2Te_3 matrix (Fig. S4 of the SM) were investigated using density functional theory calculations. In Fig. 2(e), a notable splitting of the conduction bands, as highlighted by the red box, can be observed after Zn doping. This splitting is generated by spin–orbit coupling.[49] As a result, the band degeneracy (N_v) is increased, enabling more bands to participate in effective

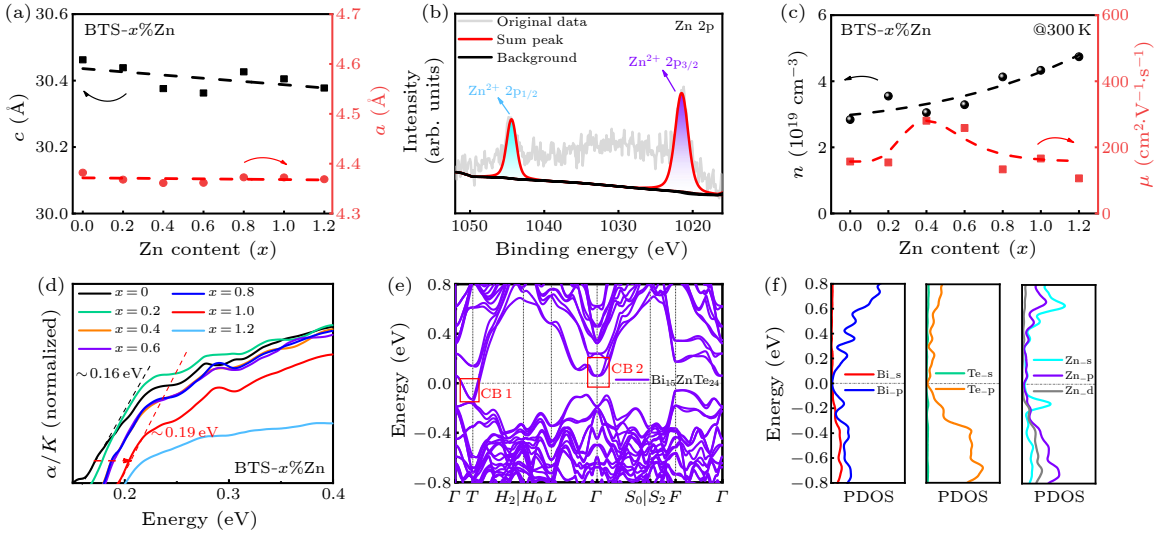

Fig. 2. (a) Lattice parameters along the a- and c-axes with varied Zn levels. (b) The XPS spectra of the Zn element in the BTS-1%Zn sample. (c) Carrier concentration n and carrier mobility μ with increasing Zn content. (d) Variation of bandgap in different BTS-x%Zn samples. (e) Calculated electronic band structure of $Bi_{15}ZnTe_{24}$. (f) PDOS for Bi, Te, and Zn orbitals.

carrier transport. Meanwhile, a band flattening effect, which is associated with a larger single-band effective mass m_b^*, can be identified in the conduction bands CB 1 and CB 2 along the L–Γ direction after Zn incorporation. This flattening effect is another factor contributing to the decrease in mobility with increasing Zn content, since m_b^* is inversely proportional to μ.

Zn incorporation modifies the electronic band structure, leading to a concerted enhancement of N_v and m_b^*. These optimizations collectively contribute to a higher S value. The projected density of states (PDOS) of constituent elements is examined to ascertain the origin of the band structure improvements. The PDOS of pure Bi_2Te_3 is shown in Fig. S5 of the SM, confirming that Te_p orbitals dominate the valence band maximum, whereas the conduction band minimum derives contributions from Bi_p and Te_p orbitals. In Zn-doped samples, the larger $\Delta\chi$ in Zn-Te compared to Bi-Te alters the bonding interactions, leading to a redistribution of electron density and modified orbital hybridization. This is reflected in the varying contributions from Bi_p and Te_p orbitals in the conduction bands [Fig. 2(f)], which can be ascribed to the activation degree of Zn_s, Zn_p, and Zn_d orbitals. These shifts in orbital composition consequently regulate the position and width of the bands, resulting in a modified electronic band structure.

Figure 3(a) displays the variation in electrical conductivity σ with respect to different Zn contents. Each sample exhibits a descending trend as temperature rises, corresponding to the characteristic of degenerate semiconductors. With Zn doping, the σ value rises to ~1152.3 S·cm^{-1} in the BTS-1.0%Zn sample, a trend attributable to changes in the dominant point defects. More specifically, these improvements are associated with the enhanced μ (~166.1 cm^2·V^{-1}·s^{-1}) and n (~4.33×10^{19} cm^{-3}). In Fig. 3(b), the negative values of the BTS-x%Zn samples demonstrate electron-dominant n-type conduction. The S values begin to deteriorate above 373 K, which is typical for narrow-bandgap Bi_2Te_3 materials owing to intrinsic bipolar excitation. Compared with the Zn-free matrix, the Zn-doped samples generally exhibit an upward trend in S values, contrasting with the conventional inverse relationship between σ and S. As a consequence, the best-performing sample, BTS-1.0%Zn, achieved a well-balanced combination of S (~−224.1 μV·K^{-1}) and σ (~1152.3 S·cm^{-1}). In addition, the typical high-temperature degradation in S has been significantly mitigated after Zn doping, with the temperature at which S_{max} occurs shifting to a higher value. This behavior is attributed to the enlarged E_g [Fig. 2(d)] and increased n introduced by Zn.

The relationship between $|S|$ and n is formulated using a single-parabolic-band model, as shown in Fig. 3(c). The density-of-states effective mass m_d^* value is ~1.45m_e for the undoped BTS matrix and rises to ~2.09m_e in BTS-1.0%Zn. This is consistent with the modification of the electronic band structure, as m_d^* is related to the band parameters via $m_d^* = N_v^{2/3} m_b^*$.[22] The observed flattened band edge and band splitting[49,50] thus optimize m_b^* and N_v, which play a crucial role in enhancing S. Due to the inherent trade-off between μ and m_d^*, the calculated μ shows a decreasing trend with increasing n [Fig. 3(d)], dropping from ~157.0 cm^2·V^{-1}·s^{-1} to ~106.3 cm^2·V^{-1}·s^{-1}. The degradation of μ can be ascribed to several factors. Firstly, Zn hinders the formation of negatively charged Bi_{Te} defects, raising n and thereby impeding carrier transport through enhanced ionized-impurity and carrier–carrier scattering. Secondly, according to the relation $\mu \propto (m_b^*)^{-3/2}(m_I^*)^{-1}$, where m_I^* represents the inertial effective mass,[51] the increase in m_b^* directly reduces μ. Finally, the evolution of dominant defects with different Zn contents also poses a substantial impact. With heavier Zn doping, the amounts of Zn_{Bi} and V_{Te} become dominant, intensifying carrier scattering and further reducing μ.

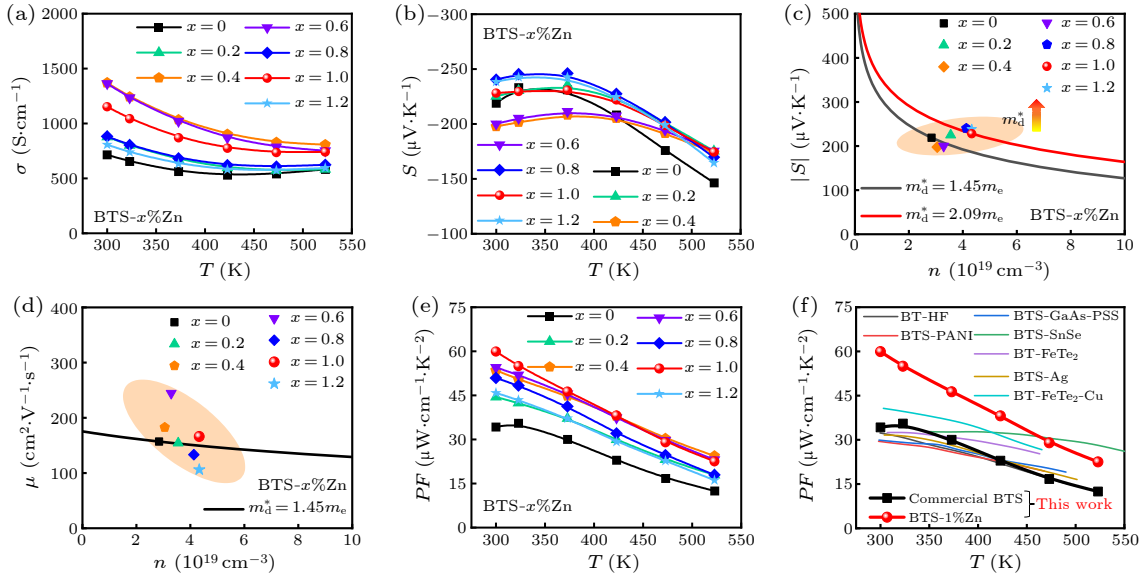

Fig. 3. Temperature-dependent electrical performance of BTS-x%Zn systems (x = 0, 0.2, 0.4, 0.6, 0.8, 1.0, and 1.2). (a) Electrical conductivity σ. (b) Seebeck coefficient S. (c) Experimental data and simulated curves with n on absolute Seebeck coefficient $|S|$ at 300 K. (d) Experimental data and simulated curves with n on carrier mobility μ at 300 K. (e) Power factor PF. (f) Comparison of PF values between this work and other n-type Bi_2Te_3-based thermoelectrics,[40,44,52–55] in which Bi_2Te_3 is abbreviated as BT and $Bi_2(Te, Se)_3$ is abbreviated as BTS.

By optimizing the interplay between μ and m_d^*, the BTS-1.0%Zn sample achieves an optimal balance, attaining an outstanding m_d^* value of $\sim 2.09 m_e$ while maintaining a moderate μ of $\sim 166.1\,cm^2 \cdot V^{-1} \cdot s^{-1}$. To further evaluate the coupling between carrier transport and electronic band structure, the weighted mobility μ_w provides a quantitative assessment. The distinct regularity in μ_w (Fig. S6 of the SM) validates the rationality of the optimization mechanism proposed here. Notably, the BTS-1.0%Zn sample exhibits a pronounced enhancement in μ_w, which reflects a favorable trade-off between S and σ values. As shown in Fig. 3(e), the maximum PF value rises from $\sim 34.2\,\mu W \cdot cm^{-1} \cdot K^{-2}$ to $\sim 60\,\mu W \cdot cm^{-1} \cdot K^{-2}$ in the BTS-1.0%Zn sample, highlighting the effective role of Zn in the n-type BTS system. A thorough PF comparison between the BTS-1.0%Zn sample and other representative n-type BTS systems [Fig. 3(f)] further underlines the exceptional advantage of the BTS-1.0%Zn system.[40,44,52–55]

2.2. Thermal Conductivity and Boosted ZT Value after Zn Doping. Based on substantially improved PF values, we further examined the thermal properties of the BTS-x%Zn. Figure 4(a) illustrates that the total thermal conductivity κ_{tot} increases with temperature T for different Zn contents. All curves exhibit an upward trend, originating from the intrinsic excitation of minority carriers. Unlike the relatively high κ_{tot} values reported in Ag/Cu-doped systems[4,9] [Fig. 1(c)], the κ_{tot} curves here present a moderate increase. The value rises from $\sim 1.2\,W \cdot m^{-1} \cdot K^{-1}$ in the pristine BTS matrix to $\sim 1.4\,W \cdot m^{-1} \cdot K^{-1}$ in the BTS-1.0%Zn, resulting from optimized n values after Zn doping. Given that $\kappa_{ele} = L\sigma T$, where L denotes the Lorentz number according to the Wiedemann–Franz law.[16] The temperature-dependent κ_{ele} values and L are plotted in Fig. S7 of the SM, together with other parameters such as the thermal diffusivity D and specific heat capacity C_p. Concerning the electron-donating role of Zn as established earlier, the increased number of electrons elevates the κ_{ele} from $\sim 0.3\,W \cdot m^{-1} \cdot K^{-1}$ (undoped BTS) to $\sim 0.6\,W \cdot m^{-1} \cdot K^{-1}$ (BTS-1.0%Zn). Since κ_{tot} comprises electronic (κ_{ele}), lattice (κ_{lat}), and bipolar (κ_{bi}) contributions, the sum of the latter two contributions is obtained by subtracting κ_{ele} from κ_{tot}[4] [Fig. 4(b)]. Similar to κ_{tot}, Zn doping mitigates the increase in thermal contributions while optimizing electrical transport performance. At the temperature range above 373 K, the $\kappa_{tot} - \kappa_{ele}$ values even exhibit a downward tendency after Zn doping. This phenomenon results from the increased concentration of point defects such as V_{Te} and Zn_{Bi} induced by doping, which is consistent with the sound velocity data in Table S1 of the SM. Besides, the adverse impact brought by bipolar diffusion has been effectively suppressed (Fig. S8 of the SM), owing to the enlarged E_g (~ 0.19 eV) and optimized n value ($\sim 4.33 \times 10^{19}\,cm^{-3}$) achieved via Zn doping.

To provide a straightforward illustration of the electron–phonon decoupling achieved by Zn incorporation, the calculated quality factor B (Fig. S9a of the SM) and deformation potential ratio ξ/ξ_0 (Fig. S9b of the SM) further serve as solid evidence. The combined enhancements in electrical performance and well-preserved thermal properties yield a competitive room-temperature dimensionless figure-of-merit ZT in BTS-1.0%Zn, which is remarkably boosted to ~ 1.3, compared to merely ~ 0.9 for the BTS matrix, representing an increment of more than 40% [Fig. 4(c)]. For the uniformity assessment of the best-performing BTS-1.0%Zn ingot, replicate measurements of key thermoelectric parameters at three spatially separated positions along the ingot were performed. The data demonstrate good reproducibility, as presented

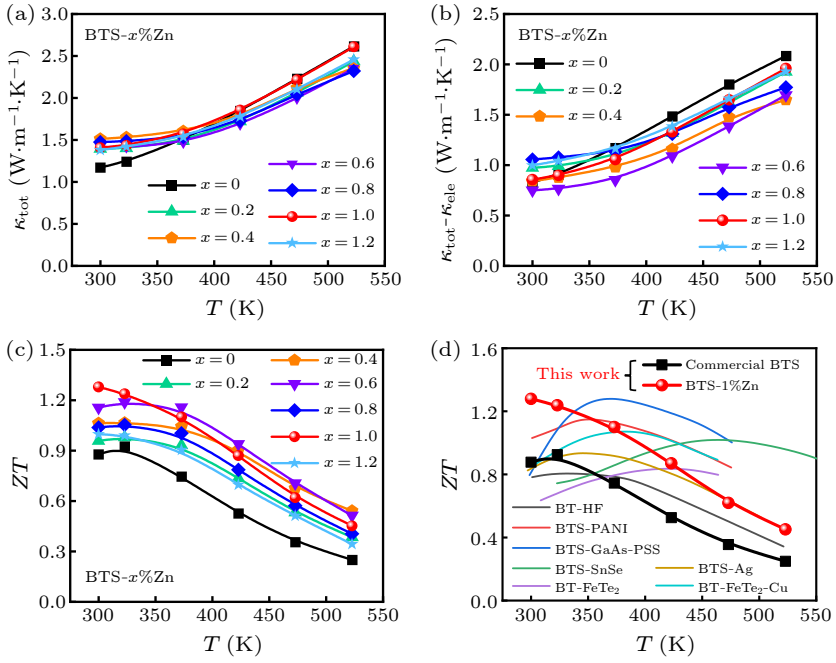

Fig. 4. Temperature-dependent thermal performance of BTS-x%Zn samples (x = 0, 0.2, 0.4, 0.6, 0.8, 1.0, and 1.2). (a) Total thermal conductivity κ_{tot}. (b) Contributions from lattice and bipolar parts: $\kappa_{tot} - \kappa_{ele}$. (c) ZT curves. (d) ZT curves of representative samples in this work compared to other n-type $Bi_2(Te,Se)_3$-based systems.[40,44,52–55]

in Fig. S10 of the SM. Additionally, a thermal cycling experiment was carried out to evaluate the stability of Zn in the BTS matrix. As shown in Fig. S11 of the SM, the BTS-1.0%Zn sample maintains stable transport properties throughout heating and cooling cycles, thus confirming its reliability for long-term service in thermoelectric devices. To further underscore the superiority of the BTS-1.0%Zn system, we compare the ZT values in this work with those reported for other n-type BTS systems[40,44,52–55] [Fig. 4(d)]. The results confirm that the BTS-1.0%Zn exhibits leading thermoelectric performance near room temperature.

2.3. Superior Performance of Thermoelectric Devices. The extraordinary room-temperature thermoelectric performance of BTS-1.0%Zn enables the fabrication of high-efficiency thermoelectric devices. The illustration in the bottom right corner of Fig. 5(a) shows a full-scale thermoelectric cooler (TEC), which is assembled by pairing the optimized n-type BTS-1.0%Zn with commercial p-type BST. The thermoelectric performance of BST is detailed in Fig. S12 of the SM. The macroscopic image of the aforementioned thermoelectric legs is provided in Fig. S13a of the SM. The exceptional structural integrity demonstrates the favorable machinability of the Zn-doped BTS system, thereby ensuring its suitability for subsequent commercial production. Furthermore, mechanical property tests reveal that BTS-1.0%Zn exhibits enhanced performance in both compressive strength and Vickers hardness (Fig. S13b of the SM), highlighting its promising prospects for large-scale deployment.

Figure 5(a) illustrates the variation of cooling temperature difference ΔT with current for various hot-side temperatures T_h. The ΔT of the BTS-1.0%Zn/BST device increases with the current I until ~5 A. The maximum cooling temperature ΔT_{max} also rises with increasing T_h. Owing to a notably high S value in BTS-1.0%Zn, a ΔT_{max} value of ~70.0 K is achieved. This value subsequently elevates to ~78.0 K and ~85.7 K when T_h is 323 K and 343 K, respectively. In contrast, the commercial BTS/BST TEC only reaches ~64.5 K, ~74.8 K, and ~84.1 K under the same T_h conditions. The corresponding cooling capacity Q_c is shown in Fig. 5(b), reaching a value as high as ~3.24 W at ΔT = 5 K. By further increasing the testing current I (Fig. S14 of the SM), the corresponding Q_c simultaneously reaches an enhanced value of ~4.73 W at I = 5 A. Concurrently, the coefficient of performance (COP) value is another critical metric for assessing the cooling performance of TECs, as a higher COP signifies greater energy efficiency.[56] The COP was tested at room temperature for various ΔT values. In Fig. 5(c), a comparison of COP between the BTS-1.0%Zn/BST and commercial BTS/BST is presented at four different ΔT values. The results illustrate a COP value of ~4.84 in the BTS-1.0%Zn/BST TEC at ΔT = 5 K, while the commercial BTS/BST only reaches ~3.29. By fixing the p-type BST material in the TEC and comparing the performance of the as-fabricated devices with those based on BTS+Ag/BST and commercial BTS/BST, we demonstrate that the strategy of optimizing the n-type BTS-Zn system provides more valuable insights into the practical improvement of device cooling capabilities. Furthermore, the ΔT_{max} of the BTS-1.0%Zn/BST is competitive, or even surpasses other leading thermoelectric modules in Fig. 5(d), including the dominant Bi_2Te_3-based, Mg-based, and Se-based TECs, underscoring its promising potential for commercial applications.[4,5,11,21,45,57–61]

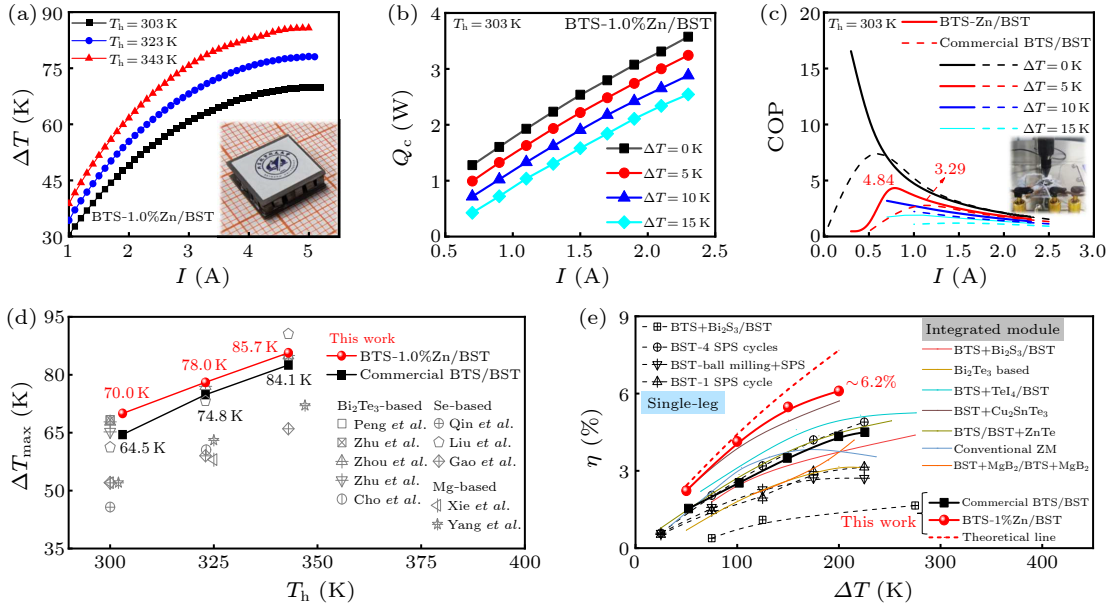

Fig. 5. The cooling and power-generating performance of the fabricated thermoelectric devices. (a) Cooling temperature difference ΔT versus current I. (b) Cooling capacity Q_c. (c) COP of the BTS-1.0%Zn/BST-based device as a function of current I under a ΔT of 0, 5, 10, 15, and 20 K, when T_h is set to 303 K. (d) Comparison of the maximum cooling temperature difference ΔT_{max} for the TECs in this study and other previous reports.[4,5,11,21,45,57–61] (e) Comparison of the maximum conversion efficiency η_{max} between this study and other reported n-type Bi_2Te_3-based devices.[19,47,62–66]

To illustrate the versatility of the BTS-1.0%Zn material in both thermoelectric refrigeration and power generation, a thermoelectric power generator (TEG) was fabricated by pairing BTS-1.0%Zn with commercial p-type BST. The curves of output voltage U, output power P, and maximum conversion efficiency η_{max} are provided in Figs. S15 and S16 of the SM. The maximum conversion efficiency can be improved by adjusting the geometric parameters, especially the length L and cross-sectional area A of the thermoelectric legs, according to the formula[67]

$$\frac{L_n A_p}{L_p A_n} = \sqrt{\frac{K_n R_p}{K_p R_n}}.$$

Herein, K and R correspond to thermal conductance and electrical resistance, respectively. With the leg length fixed at 5 mm, the optimal A_p/A_n was calculated as ~1.1 based on attained transport properties. The measured curves of the energy conversion efficiency parameters are provided in Fig. S15 of the SM. The slope of the U–I curves implies the internal resistance of the TEG, increasing from ~0.3 Ω to ~0.4 Ω when the ΔT value increases from 50 K to 200 K, consistent with the degradation of σ at higher temperatures. Correspondingly, the maximum output voltage U_{max} rises from ~0.15 V to ~0.55 V over the same temperature range. For comparison, the U–I curves of the commercial BTS/BST are also shown in Fig. S16 of the SM, with a U_{max} value of only ~0.13 V at ΔT = 50 K and ~0.47 V at ΔT = 200 K. The P–I results further illustrate the advantageous performance of the BTS-1.0%Zn/BST, achieving a P_{max} of ~0.35 W, much higher than the ~0.20 W obtained from the unoptimized TEG. Under vacuum conditions, the Zn-doped devices reach a η_{max} value of ~6.2% with a ΔT of 200 K, superior to the commercial BTS/BST TEG ($\eta_{max} \approx 4.3\%$). Moreover, the theoretically calculated η curves have also been included here for comparison. The results indicate that practical TEGs are subject to various energy losses and deviations from ideal operating conditions, which account for the underestimation of the measured efficiency curves relative to the theoretical line. A comparative analysis of η_{max} involving single-leg and integrated modules[19,47,62–66] is exhibited in Fig. 5(e), emphasizing the exceptional performance of the BTS-1.0%Zn/BST.

3. Conclusion. In summary, this work demonstrates a straightforward and highly effective approach for the decoupling of electrical parameters in n-type Bi_2Te_3-based thermoelectric materials. Incorporating Zn into commercial BTS enables the cooperative optimization of band structures and defect configurations. Specifically, Zn atoms preferentially substitute Bi sites, increasing the electron concentration. Simultaneously, Zn doping induces multi-level band modulations—including bandgap widening, band flattening, and splitting—which collectively enhance the Seebeck coefficient without compromising electrical conductivity. These synergistic effects lead to a noteworthy improvement in PF values (~60 μW·cm^{-1}·K^{-2} at 300 K) while maintaining a moderate thermal conductivity. Consequently, an ultra-high ZT value of ~1.3 is achieved in BTS-1.0%Zn at room temperature. Full-scale thermoelectric modules fabricated using the optimized BTS-1.0%Zn exhibit remarkable performance in both cooling and power generation. Notably, an outstanding maximum cooling temperature difference ΔT_{max} of ~70.0 K at room temperature and a maximum conversion efficiency η_{max} of ~6.2% (ΔT = 200 K) are attained. These results underscore the promising prospects of Zn-doped BTS

in high-efficiency solid-state cooling and low-grade heat harvesting.

Acknowledgements. This work was supported by the National Key Research and Development Program of China (Grant No. 2024YFA1210400), the National Science Fund for Distinguished Young Scholars (Grant No. 52525101), the National Natural Science Foundation of China (Grant Nos. 52450001 and 22409014), the International Cooperation and Exchange of the National Natural Science Foundation of China (Grant No. 52411540237), and the Tencent Xplorer Prize. B.C.Q. acknowledges the support of the National High-Level Talent Special Support Programs—Young Talents.

References

[1] Bai S L, Qin B C, and Zhao L D 2025 *J. Chin. Ceram. Soc.* **53** 733 (in Chinese)
[2] Tian Y, Qin B C, Li J N, and Zhao L D 2025 *Sci. Bull.* **70** 3466
[3] Hu Y X, Bai S L, Qin B C, and Zhao L D 2025 *Electromag. Sci.* **3** 0100611
[4] Peng J Y, Liu D R, Bai S L, Wen Y, Liang H Q, Su L Z, Qian X, Wang D Y, Gao X, Ding Z H, Cao Q, Pei Y L, Qin B C, and Zhao L D 2025 *Adv. Energy Mater.* **15** 2404653
[5] Zhang Z Y, Si Z, Wei Y X, Wen Y, Kang J K, Chen P P, Li Y C, Hu Y X, Peng J Y, Jin Y, Liu S B, Shi H N, Gao X, Gao D Z, Xie H Y, and Zhao L D 2025 *Adv. Energy Mater.* **15** 2501184
[6] Qin Y X, Qin B C, Hong T, Zhang X, Wang D Y, Liu D R, Wang Z Y, Su L Z, Wang S N, Gao X, Ge Z H, and Zhao L D 2024 *Science* **383** 1204
[7] Gao T, Wen Y, Bai S L, Su L Z, Shi H N, Liu R, Wang S N, Hu Y X, Liu S B, Liu D R, Liu S, Liang C, Feng X K, Wang X Q, Qin Y X, Gao X, Qin B C, Chang C, Bai P K, and Zhao L D 2025 *Science* **390** 1266
[8] Zhu H, Deng Z M, Qu Y H, He P, and Geng H Y 2025 *Adv. Funct. Mater.* **35** 2422007
[9] Liu D R, Bai S L, Wen Y, Peng J Y, Liu S B, Shi H N, Li Y C, Hong T, Liang H Q, Qin Y X, Su L Z, Qian X, Wang D Y, Gao X, Ding Z H, Cao Q, Tan Q, Qin B C, and Zhao L D 2025 *Natl. Sci. Rev.* **12** nwae448
[10] Wang S Q, Bai S L, Chen P P, Zhan S P, Tian Y, Wang L, Liu D R, Peng J Y, Li Y C, Gao D Z, Gao T, Zhang Z Y, Si Z, Wei Y X, Xie H Y, Gao X, Zhu Y C, Wen Y, and Zhao L D 2025 *J. Am. Chem. Soc.* **147** 15827
[11] Qin B C, Wang D Y, Liu X X, Qin Y X, Dong J F, Luo J F, Li J W, Liu W, Tan G J, Tang X F, Li J F, He J Q, and Zhao L D 2021 *Science* **373** 556
[12] Jia F, Yin X, Cheng W W, Lan J T, Zhan S H, Chen L, and Wu L M 2023 *Angew. Chem. Int. Ed.* **62** e202218019
[13] Kumar R, Bhatt R, Tewary A, Debnath A K, Bhatt P, Mani N, Jha P, Patro P, Bhattacharya S, Pathak M, Khan M K, Singh A, and Muthe K P 2022 *J. Mater. Chem. C* **10** 7970
[14] Shenoy U S and Bhat D K 2024 *J. Phys. Chem. Solids* **188** 111943
[15] Zhang X, Kang J, and Wei S H 2024 *Chin. Phys. Lett.* **41** 026301
[16] Wu G, Zhang Q, Tan X J, Fu Y T, Guo Z, Zhang Z W, Sun Q Q, Liu Y, Shi H L, Li J S, Noudem J G, Wu J H, Liu G Q, Sun P, Hu H Y, and Jiang J 2024 *Adv. Mater.* **36** 2400285
[17] Mansoor A, Jabar B, Shah S S A, Javed M S, Najam T, Ishaq M, Chen S, Li F, Shi X L, Chen Y X, Liang G X, Chen Z G, and Zheng Z H 2025 *Energy Environ. Sci.* **18** 2485
[18] Jiang L F, Tan S Y, Chen R C, Xian J W, Li H R, Zhou D H, Kang H J, Chen Z N, Guo E Y, and Wang T M 2024 *ACS Appl. Mater. Interfaces* **16** 60197
[19] Pan Q Y, Pang K K, Zhang Q, Liu Y, Shi H L, Li J S, Zhou W J, Sun Q Q, Zhang Y Y, Tan X J, Sun P, Wu J H, Liu G Q, and Jiang J 2024 *J. Mater. Chem. A* **12** 8785
[20] Deng T T, Gao Z Q, Li Z, Qiu P F, Li Z, Yuan X J, Ming C, Wei T R, Chen L D, and Shi X 2024 *Science* **386** 1112
[21] Liu D R, Bai S L, Tian Y, Peng J Y, Liu S B, Shi H N, Liang H Q, Qin Y X, Su L Z, Qian X, Qin B C, and Zhao L D 2025 *Adv. Mater.* **32** 2506999
[22] Qin B C, Kanatzidis M G, and Zhao L D 2024 *Science* **386** eadp2444
[23] Qin B C, Wang D Y, Hong T, Wang Y P, Liu D R, Wang Z Y, Gao X, Ge Z H, and Zhao L D 2023 *Nat. Commun.* **14** 1366
[24] Shi H N, Wen Y, Bai S L, Chang C, Su L Z, Gao T, Liu S B, Liu D R, Qin B C, Qin Y X, Liang H Q, Qian X, Hou Z H, Gao X, Zhou T H, Tan Q, and Zhao L D 2025 *Nat. Commun.* **16** 1788
[25] Zhang X Y, Wan Y Y, Wen Y, Zhu Y C, Liu H, Qiu J X, Zhu Z P, Sun Z T, Gao X, Bai S L, Zhang Y Q, Zhang L, Yan X H, Zhang J M, Liu Y, Li S, and Zhao L D 2025 *Nat. Catal.* **8** 465
[26] Liu D R, Wang D Y, Hong T, Wang Z Y, Wang Y P, Qin Y X, Su L Z, Yang T Y, Gao X, Ge Z H, Qin B C, and Zhao L D 2023 *Science* **380** 841
[27] Li D, Hu Y X, Zhang H P, Zhang G, and Li D F 2025 *Chin. Phys. Lett.* **42** 120710
[28] Tao H, Gao D Z, Wen Y, Peng J Y, Tan Q, and Zhao L D 2025 *Adv. Funct. Mater.* **35** 2511682
[29] Gao D Z, Wen Y, Bai S L, Wang S Q, Liu S B, Li Y C, Wang L, Zang W J, Su X L, Gao X, Xie H Y, and Zhao L D 2024 *Small* **20** 2407556
[30] Wang L, Wen Y, Bai S L, Chang C, Li Y C, Liu S, Liu D R, Wang S Q, Zhao Z, Zhan S P, Cao Q, Gao X, Xie H Y, and Zhao L D 2024 *Nat. Commun.* **15** 3782
[31] Jiao W Y, Yuan H M, Han S H, Luo Y F, Cao H B, and Liu H J 2025 *Chin. Phys. Lett.* **42** 080603
[32] Hu Y X, Bai S L, Wen Y, Liu D R, Hong T, Liu S, Zhan S P, Gao T, Chen P P, Li Y C, Wang L, Gao D Z, Gao X, Tan Q, Qin B C, and Zhao L D 2025 *Adv. Funct. Mater.* **35** 2414881
[33] Liu S, Bai S L, Wen Y, Lou J, Jiang Y Z, Zhu Y C, Liu D R, Li Y C, Shi H N, Liu S B, Wang L, Zheng J Q, Zhao Z, Qin Y X, Liu Z K, Gao X, Qin B C, Chang C, and Zhao L D 2025 *Science* **387** 202
[34] Jin Y, Qiu Y T, Pan C F, and Zhao L D 2025 *Adv. Mater.* **37** 2500802
[35] Cai Z T, Fang Y, Ma C, Zheng K P, Lei K, Ke S M, Zheng R K, and Li H 2024 *ACS Appl. Mater. Interfaces* **16** 64868
[36] Jin Y, Qiu Y T, Bai S L, Xie H Y, Liu S B, Hong T, Gao X, Wen Y, and Zhao L D 2024 *Adv. Energy Mater.* **14** 2400623
[37] Jin Y, Wang D Y, Hong T, Su L Z, Shi H N, Zhan S P, Wang Y P, Wang S N, Gao X, Qiu Y T, and Zhao L D 2022 *Adv. Energy Mater.* **12** 2103779
[38] Du J Y, Sun Y X, Guo F K, Tong H Y, Yu Z Y, Liu Z H, Zhu J B, and Sui J H 2025 *Mater. Today Phys.* **53** 101705
[39] Feng J H, Yang P, Li A L, Li H, Min E B, Li F J, Zhang H C, Li J, Zhao P Y, Sun R, and Liu R H 2025 *Acta Mater.* **295** 121185
[40] Chen T, Li S J, Wang Z Y, Ge Z H, Zhang Y S, Xin H X, Li D, Zhang J, and Qin X Y 2025 *Small* **21** 2406695

[41] Zhang F D, He M K, Zhu L J, Jia B Q, Shi Y L, Wang W S, Peng Z H, Liang P F, Chao X L, Yang Z P, and Wu D 2024 *Small* **20** 2405182

[42] Luo K Y, Chen H W, Hu W Y, Qian P P, Guo J B, Deng Y X, Yang L, Sun Q, Liu L, Cao L, Qiu W B, and Tang J 2024 *Nano Energy* **128** 109845

[43] Jin K P, Yang Z Y, Fu L W, Lou Y, Xu P F, Huang M, Shi Z, and Xu B 2024 *ACS Nano* **18** 13924

[44] Zhu Y K, Jin Y F, Zhu J B, Dong X Y, Liu M, Sun Y X, Guo M C, Li F S, Guo F K, Zhang Q, Liu Z H, Cai W, and Sui J H 2023 *Adv. Sci.* **10** 2206395

[45] Zhu Y K, Sun Y X, Dong X Y, Yin L, Liu M, Guo M C, Wu H, Li F S, Guo Z T, Wang X Y, Yu K, Guo F K, Zhang Q, Liu Z H, Cai W, and Sui J H 2024 *Joule* **8** 193

[46] Xiong Q H, Han G, Wang G Y, Lu X, and Zhou X Y 2024 *Adv. Funct. Mater.* **34** 2411304

[47] Deng R G, Su X L, Hao S Q, Zheng Z, Zhang M, Xie H Y, Liu W, Yan Y G, Wolverton C, Uher C, Kanatzidis M G, and Tang X F 2018 *Energy Environ. Sci.* **11** 1520

[48] Yun Y H, An E J, and Jeong Y J 2023 *Mater. Lett.* **346** 134499

[49] Bai S L, Hu Y X, Zhan S P, Gao T, Qin B C, and Zhao L D 2025 *J. Am. Chem. Soc.* **147** 27059

[50] Bai S L, Shi H N, Wen Y, Hu Y X, Zheng J Q, Qin Y X, Su L Z, Liu S B, Liu D R, Gao T, Hong T, Gao X, Zhu F Y, Qin B C, and Zhao L D 2025 *Phys. Rev. X* **15** 031033

[51] Qin B C and Zhao L D 2022 *Mater. Lab* **1** 220004

[52] Yang S H, Ming H W, Li D, Chen T, Li S J, Zhang J, Xin H X, and Qin X Y 2023 *Chem. Eng. J.* **455** 140923

[53] Song C C, Shi X L, Pan L, Liu W D, Sun Q, Li M, Lu C H, Liu Q F, Wang Y F, and Chen Z G 2023 *Acta Mater.* **254** 119023

[54] Rahman J U, Nam W H, Jung Y J, Won J H, Oh J M, Van Du N, Rahman G, García-Suárez V M, He R, Nielsch K, Cho J Y, Seo W S, Roh J W, Kim S, Lee S, Lee K H, Kim H S, and Shin W H 2024 *Energy Environ. Mater.* **7** e12663

[55] Li L, Wei P, Yang M J, Zhu W T, Nie X L, Zhao W Y, and Zhang Q J 2023 *Sci. China Mater.* **66** 3651

[56] Xu S D, Horta S, Lawal A, Maji K, Lorion M, and Ibáñez M 2025 *Science* **387** 845

[57] Zhu W, Wei P, Zhang J Q, Li L Z, Zhu W T, Nie X L, Sang X H, Zhang Q J, and Zhao W Y 2022 *ACS Appl. Mater. Interfaces* **14** 12276

[58] Zhou J, Feng J H, Li H, Liu D, Qiu G J, Qiu F, Li J, Luo Z Z, Zou Z G, Sun R, and Liu R H 2023 *Small* **19** 2300654

[59] Cho H, Yun J H, Back S Y, Lee J S, Kang N, Jang Y I, Lim J, Son J H, Park J Y, Kim J, Joo M, and Rhyee J S 2021 *J. Alloys Compd.* **888** 161572

[60] Yang J W, Li G D, Zhu H T, Chen N, Lu T B, Gao J L, Guo L W, Xiang J S, Sun P J, Yao Y, Yang R G, and Zhao H Z 2022 *Joule* **6** 193

[61] Xie L J, Yang J W, Liu Z Y, Qu N, Dong X Y, Zhu J B, Shi W J, Wu H, Peng G Y, Guo F K, Zhang Y, Cai W, Wu H J, Zhu H T, Zhao H Z, Liu Z H, and Sui J H 2023 *Mater. Today* **6** 55

[62] Qiu J H, Yan Y G, Luo T T, Tang K C, Yao L, Zhang J, Zhang M, Su X L, Tan G J, Xie H Y, Kanatzidis M G, Uher C, and Tang X F 2019 *Energy Environ. Sci.* **12** 3106

[63] Zhang C H, Lai Q W, Wang W, Zhou X Y, Lan K L, Hu L P, Cai B W, Wuttig M, He J Q, Liu F S, and Yu Y 2023 *Adv. Sci.* **10** 2302688

[64] Zhu Y K, Sun Y X, Zhu J B, Song K, Liu Z H, Liu M, Guo M C, Dong X Y, Guo F K, Tan X J, Yu B, Cai W, Jiang J, and Sui J H 2022 *Small* **18** 2201352

[65] Hu X K, Nagase K, Jood P, Ohta M, and Yamamoto A 2015 *J. Electron. Mater.* **44** 1785

[66] Zhuang H L, Pei J, Cai B W, Dong J F, Hu H H, Sun F H, Pan Y, Snyder G J, and Li J F 2021 *Adv. Funct. Mater.* **31** 2009681

[67] Zhang Q, Yuan M H, Pang K K, Zhang Y Y, Wang R Y, Tan X J, Wu G, Hu H Y, Wu J H, Sun P, Liu G Q, and Jiang J 2023 *Adv. Mater.* **35** 2300338